molecules

MDPI

Article

Effect of Equivalence Ratio on Pollutant Formation in $CH_4O/H_2/NH_3$ Blend Combustion

Jingyun Sun [1], Qianqian Liu [1], Mingyan Gu [1] and Yang Wang [1,2,*]

[1] School of Energy and Environment, Anhui University of Technology, Ma'anshan 243002, China; jingyunsun133@163.com (J.S.); liuqianqian208dw@163.com (Q.L.); gumy@ahut.edu.cn (M.G.)
[2] School of Materials Science and Engineering, Anhui University of Technology, Ma'anshan 243032, China
* Correspondence: wangyang@ahut.edu.cn; Tel.: +86-055-5231-1816

Abstract: This paper investigates the effect of equivalence ratio on pollutant formation characteristics of $CH_4O/H_2/NH_3$ ternary fuel combustion and analyzes the pollutant formation mechanisms of CO, CO_2, and NO_X at the molecular level. It was found that lowering the equivalence ratio accelerates the decomposition of CH_4O, H_2, and NH_3 in general. The fastest rate of consumption of each fuel was found at $\varphi = 0.33$, while the rates of CH_4O and NH_3 decomposition were similar for the $\varphi = 0.66$ and $\varphi = 0.4$. CO shows an inverted U-shaped trend with time, and peaks at $\varphi = 0.5$. The rate and amount of CO_2 formation are inversely proportional to the equivalence ratio. The effect of equivalence ratio on CO_2 is obvious when $\varphi > 0.5$. NO_2 is the main component of NO_X. When $\varphi < 0.66$, NO_X shows a continuous increasing trend, while when $\varphi \geq 0.66$, NO_X shows an increasing and then stabilizing trend. Reaction path analysis showed that intermediates such as CH_3 and CH_4 were added to the CH_4O to CH_2O conversion stage as the equivalence ratio decreased with $\varphi \geq 0.5$. New pathways, $CH_4O \rightarrow CH_3 \rightarrow CH_2O$ and $CH_4O \rightarrow CH_3 \rightarrow CH_4 \rightarrow CH_2O$, were added. At $\varphi \leq 0.5$, new intermediates CHO_2 and CH_2O_2 were added to the CH_2O to CO_2 conversion stage, and new pathways are added: $CH_2O \rightarrow CO \rightarrow CHO_2 \rightarrow CO_2$, $CH_2O \rightarrow CO \rightarrow CO_2$, $CH_2O \rightarrow CHO \rightarrow CO \rightarrow CHO_2 \rightarrow CO_2$, and $CH_2O \rightarrow CH_2O_2 \rightarrow CO_2$. The reduction in the number of radical reactions required for the conversion of NH_3 to NO from five to two directly contributes to the large amount of NO_X formation. Equivalent ratios from 1 to 0.33 corresponded to 12%, 21.4%, 34%, 46.95%, and 48.86% of NO_2 remaining, respectively. This is due to the fact that as the equivalence ratio decreases, more O_2 collides to form OH and some of the O_2 is directly involved in the reaction forming NO_2.

Keywords: ternary blend combustion; equivalent ratio; NO_X; ReaxFF MD; reaction mechanism

Citation: Sun, J.; Liu, Q.; Gu, M.; Wang, Y. Effect of Equivalence Ratio on Pollutant Formation in $CH_4O/H_2/NH_3$ Blend Combustion. *Molecules* **2024**, *29*, 176. https://doi.org/10.3390/molecules29010176

Academic Editor: Maxim L. Kuznetsov

Received: 28 November 2023
Revised: 25 December 2023
Accepted: 25 December 2023
Published: 28 December 2023

1. Introduction

Currently, the global transportation industry relies mainly on fossil energy sources [1], but the combustion of these traditional fossil energy sources causes a lot of pollution. Clean, efficient, and sustainable are the current trends in energy development [2,3]. Hydrogen and ammonia are both ideal clean and renewable fuels, which have received extensive attention from scholars at home and abroad. Hydrogen is renewable and characterized by good combustibility, low ignition energy, and fast combustion speed [4,5]. However, the difficulties in storing and transporting hydrogen, the premature ignition and backfire caused by overly fast combustion speeds, and the high combustion temperature that produces NO_X pollution have all limited the practical popularization of the use of pure hydrogen fuel [6]. Ammonia, as a good zero-carbon hydrogen storage carrier, can be obtained from biomass or other renewable sources. It is considered a sustainable fuel that can be transported and applied remotely [7]. Currently, ammonia is widely used as a fuel in automobile engines [8], marine engines [9], and generator internal combustion engines [10], where the low viscosity of ammonia helps in fuel atomization and droplet formation during fuel injection [11]. Ammonia also has a high octane rating, which makes it suitable for engines

with high compression ratios and reduced detonation [12]. However, the disadvantages of ammonia's low combustion rate [13] and high auto-ignition temperature [14], as well as narrow combustible limits, tend to lead to incomplete combustion, which results in poor engine performance. Therefore, it is difficult to use as a single fuel for direct combustion [15,16]. The use of hydrogen as a combustion aid and ammonia miscombustion was found to be one of the ways to improve ammonia combustion efficiency [17]. This not only leads to improved in-cylinder combustion [18] but also reduces the requirement for engine modifications (material compatibility), thus ensuring a cost-effective transition to hydrogen energy [19]. Wang et al. [20] found that engine exhaust heat can crack some of the ammonia into hydrogen and nitrogen to form reformed gases, making this method much more maneuverable. A study by Alam et al. [21] indicated that although hydrogen–ammonia blending can reduce carbon emissions including CO and others in diesel internal combustion engines, incomplete combustion of the fuel and higher NO_X emission phenomena were observed.

Blending oxygenated fuels as a combustion aid is also an effective way to improve combustion performance and pollutant emissions in diesel engines [22,23]. Methanol, as the saturated monohydric alcohol with the simplest structure, is inexpensive and simple to synthesize. It is a high-quality representative for studying the combustion-enhancing effect of oxygenated fuels [24,25]. Methanol is ideal for fuel-lean combustion. However, obtaining high energy and reliable ignition is one of the biggest challenges of fuel-lean combustion [26]. The reformed gas in the engine can provide exactly this energy due to the presence of H_2. Li et al. [27] investigated the ignition delay time of ammonia/methanol blends with equivalence ratios of 0.5, 1.0, and 2.0 and temperatures in the temperature range of 1250–2150 K. The results showed that the ignition delay time of ammonia/methanol blends was mainly affected by free radicals such as OH, O, HO_2, and H. Li et al. [28] found that blending a small amount of methanol into ammonia combustion made the blend more reactive due to the fact that the addition of methanol introduced a new reaction sequence, $CH_3OH \rightarrow CH_2OH/CH_3O \rightarrow CH_2O \rightarrow CHO$, which enriched the O/H radical library.

However, there are very few studies on $CH_4O/H_2/NH_3$ blend combustion. Given the complexity of engine in-cylinder combustion and pollutant formation characteristics, it is not conducive to the isolated exploration of chemical reaction kinetics and mixed fuel combustion pollutant laws under different operating parameters [29]. This leads to the fact that the mechanism of blended combustion action is not yet well clarified.

2. Results and Discussion

2.1. Effect of Equivalent Ratio on Combustion Components of Ternary Carbon-Neutral Fuel Blends

Figure 1 shows the effect of different equivalence ratios on the four reactant components, CH_4O, NH_3, H_2, and O_2, during the blended combustion process of ternary carbon-neutral fuels. Lowering the equivalence ratio accelerates the decomposition of CH_4O, NH_3, and H_2 in general. As the equivalence ratio is lowered, the decomposition rate of CH_4O is the fastest at $\varphi = 0.33$ throughout the reaction. As the reaction proceeds, the decomposition rate of the $\varphi = 0.5$ condition becomes progressively higher, gradually replacing the $\varphi = 0.4$ condition. At this time, the decomposition rate of CH_4O was similar between $\varphi = 0.4$ and $\varphi = 0.66$. The decomposition rate of NH_3 increased linearly with the decrease in the equivalence ratio, and the consumption rate of O_2 increased with the increase in the equivalence ratio when $\varphi \leq 0.5$, and its consumption rate was the smallest when $\varphi = 0.4$. The curves of H_2 showed a similar trend to that of CH_4O, and the highest consumption rate was found in the case of $\varphi = 0.33$; this was next to that in the case of $\varphi = 0.5$, but it was different from that of $\varphi = 0.4$. $\varphi = 0.4$ is not notably different.

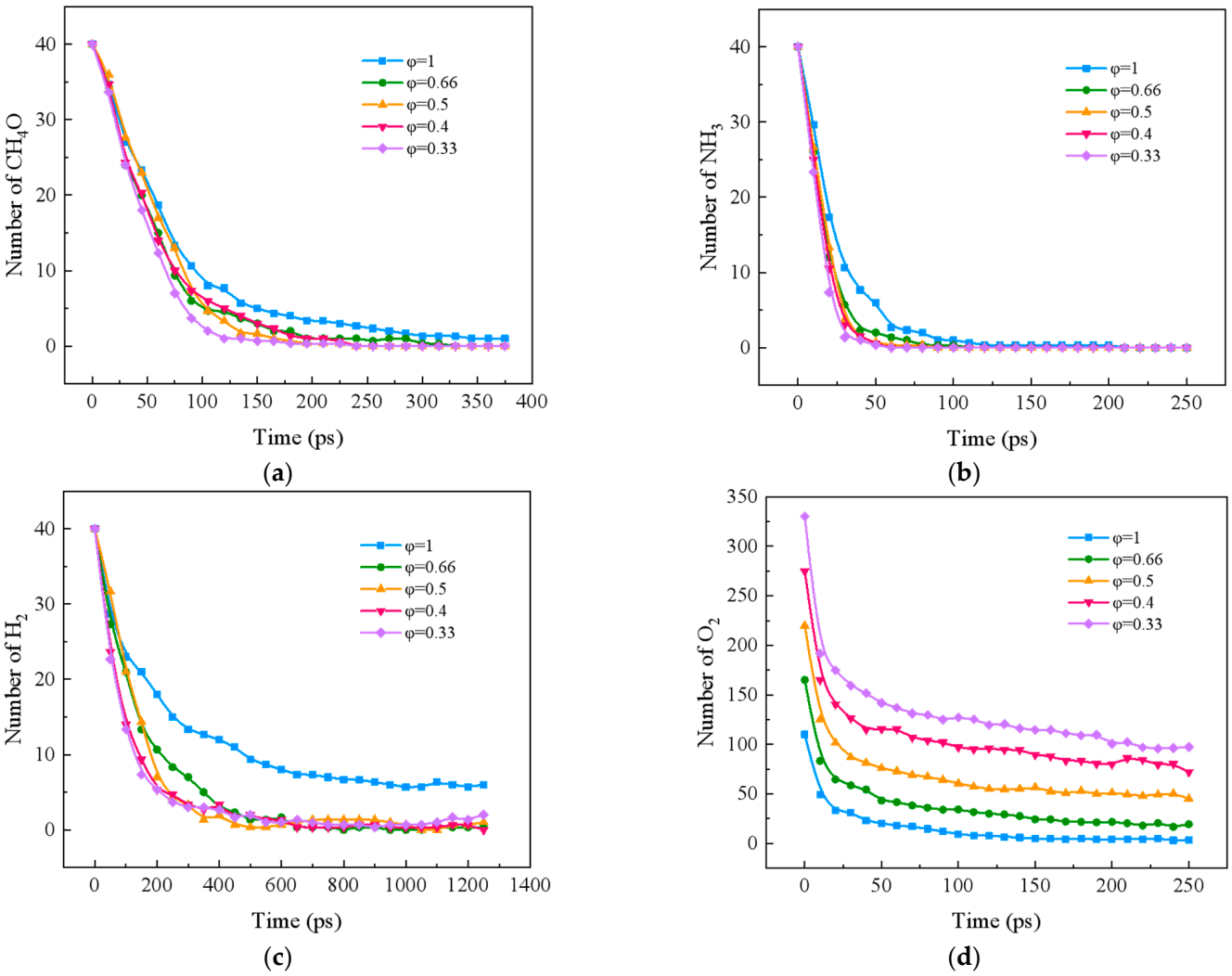

Figure 1. Changes in reactants during combustion of carbon-neutral fuels with different equivalence ratios. (**a**) CH_4O; (**b**) NH_3; (**c**) H_2; (**d**) O_2.

Figure 2 shows the variation of major products and radicals during combustion of ternary carbon-neutral fuels at different equivalence ratios. Figure 2a indicates that there is almost no change in N_2 with time for different equivalence ratios. Only N_2 at $\varphi = 1$ has an increase, and the decreasing trend of N_2 becomes more and more obvious as the equivalence ratio decreases at $\varphi \leq 0.66$. This is because at a reaction temperature of 2000 K, oxygen becomes more and more abundant as the equivalence ratio decreases, and more N_2 reacts with O to produce more thermodynamic NO_X. Figure 2b shows the trend of H_2O over time. There is no strict linear relationship between the amount of H_2O generated and the equivalence ratio. The maximum amount of H_2O is generated at $\varphi = 0.66$, and there is little difference between $\varphi = 1$ and $\varphi = 0.5$.

Figure 2c,d show the effect of different equivalence ratios on the formation of OH and H during the blending process of ternary carbon-neutral fuels, respectively. Comparing the two figures, it can be seen that the effect of equivalence ratio on OH is more pronounced. OH increases rapidly and then decreases slowly as time progresses. The higher the equivalence ratio, the higher the amount of low OH. OH may be the key radical leading to the depletion of CH_4O, H_2, and NH_3. This conclusion will be confirmed in Section 2.3. The H curve shows a tendency to rise and then fall, with a small but fluctuating overall number. The peak occurs at $\varphi = 0.66$. H also assumes an important role in the reaction.

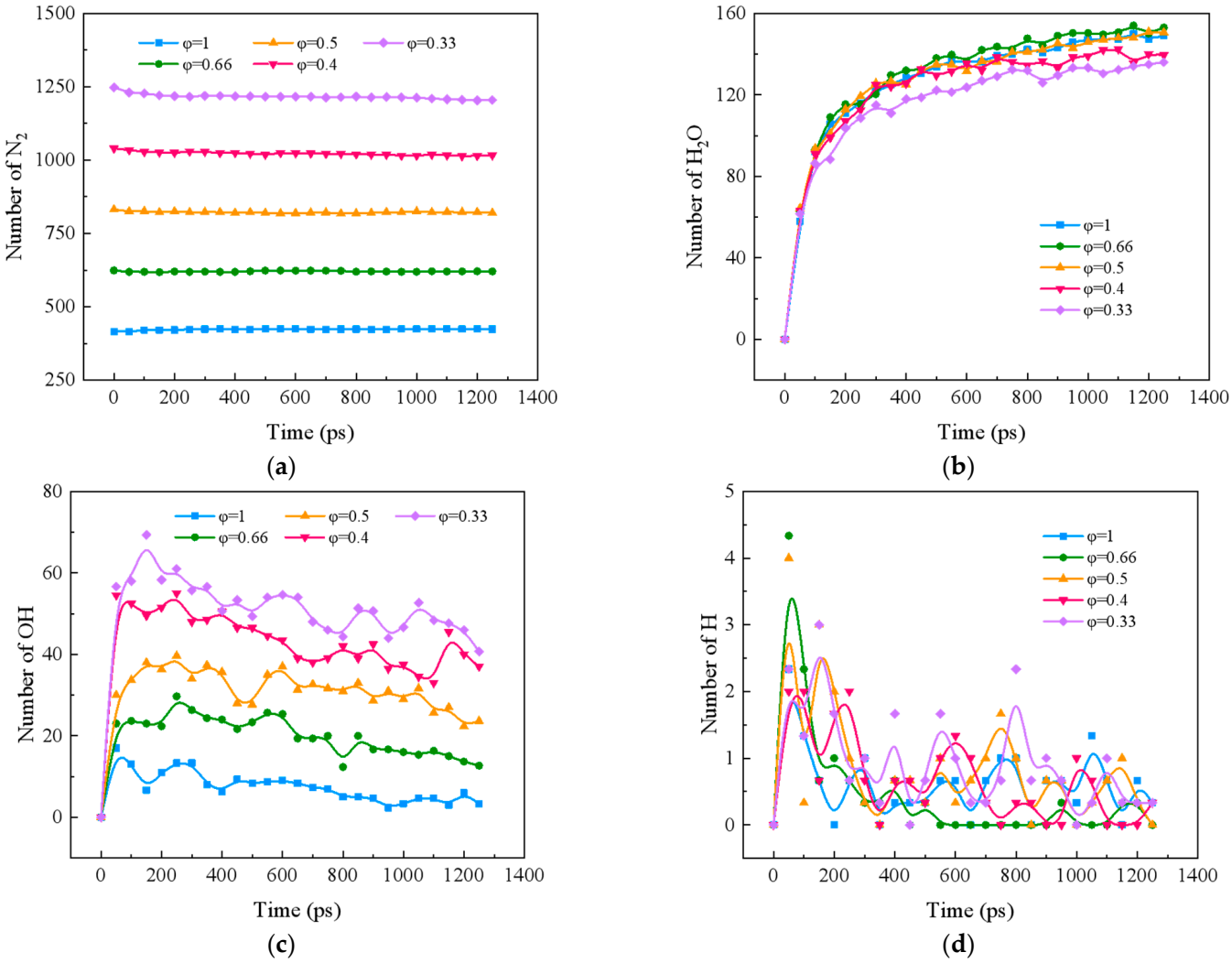

Figure 2. Changes of components and radicals during combustion at different temperatures. (**a**) N_2; (**b**) H_2O; (**c**) OH; (**d**) H.

2.2. Effect of Equivalence Ratio on Pollutant Formation in Blended Combustion of Ternary Carbon-Neutral Fuels

2.2.1. Effect of Equivalent Ratio on CO and CO_2 Formation in Blended Combustion of Ternary Carbon-Neutral Fuels

Figure 3a shows the formation of CO during the blending process of ternary carbon-neutral fuels at different equivalence ratios. CO shows an inverted U-shape trend with time, the peak value of CO shifts backward with the increase in the equivalence ratio, and the rate of CO formation increases with the decrease in the equivalence ratio in the early stage of the reaction. The CO peaks were 9.33, 8.67, 9.67, 9.33, and 8.67 for the equivalence ratios from 1 to 0.33, respectively. The maximum CO peak was observed at φ = 0.5. This may be due to the fact that there is more CO production and less CO consumption at φ = 0.5. The detailed pathway analysis will be carried out at the molecular level in Section 2.3 for the specific causes.

Figure 3b shows the CO_2 formation during the combustion of ternary carbon-neutral fuel blends with different equivalence ratios. The CO_2 formation rate and amount are inversely proportional to the size of the equivalence ratio. The equivalence ratio has little effect on the amount of CO_2 when $\varphi \leq 0.5$. When the equivalence ratio $\varphi > 0.5$, the effect of the equivalence ratio on CO_2 is more obvious.

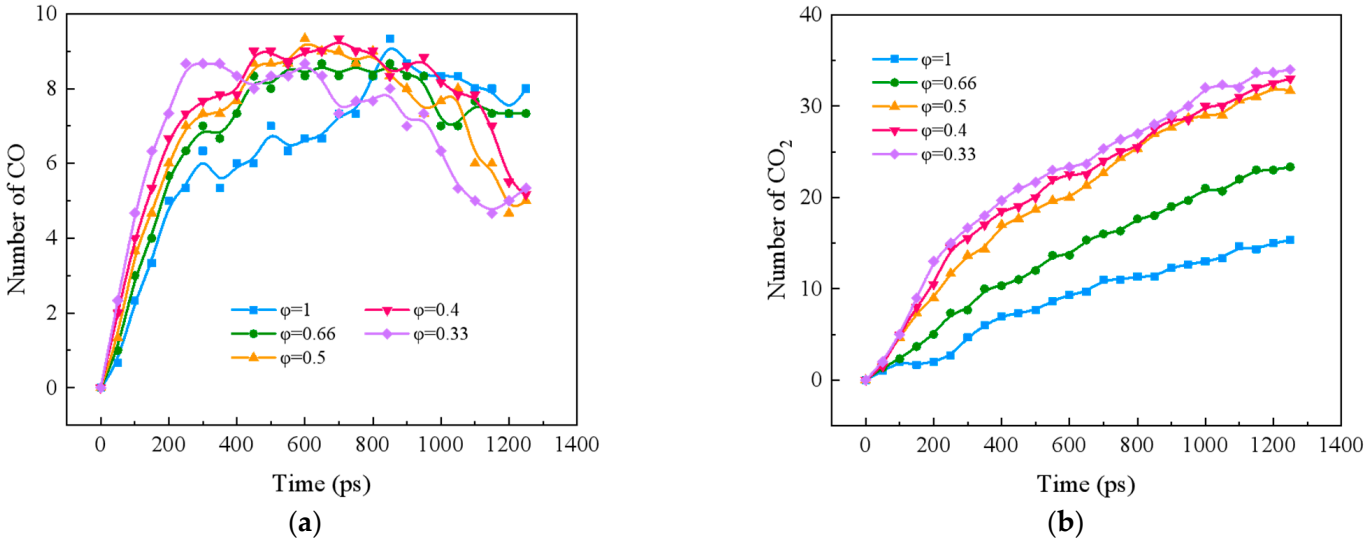

Figure 3. CO and CO_2 formation with time for blended combustion. (**a**) CO; (**b**) CO_2.

2.2.2. Effect of Equivalent Ratio on NO_X Formation in Blended Combustion of Ternary Carbon-Neutral Fuels

Figure 4 shows the effect of equivalence ratio on the formation of NO_X (NO, NO_2, and NO_3) in the combustion of ternary carbon-neutral fuel blends. From Figure 4a, it can be seen that as the combustion proceeds, NO shows a trend of rapid increase followed by a slow decrease. The peak value of NO increases with the decrease in the equivalence ratio. From Figure 4b,c, it can be seen that both NO_2 and NO_3 gradually increase with the reaction; NO_2 is the main component of NO_X. NO_3 shows an overall trend of increasing and then slowly decreasing, and the peak value increases with the decrease in the equivalence ratio, and the peak time is also delayed. In the middle and late stages of the reaction, NO_3 at $\varphi = 0.33$ was significantly higher than other working conditions.

As can be seen from Figure 4d, when $\varphi \geq 0.66$, NO_X shows a tendency to increase and then stabilize as the reaction proceeds. When $\varphi < 0.66$, NO_X shows a continuous growth trend. and the growth rate decreases around 200ps. However, the NO_X growth rate in the middle and late stages when $\varphi < 0.44$ is significantly higher than that in the case of $\varphi \geq 0.44$.

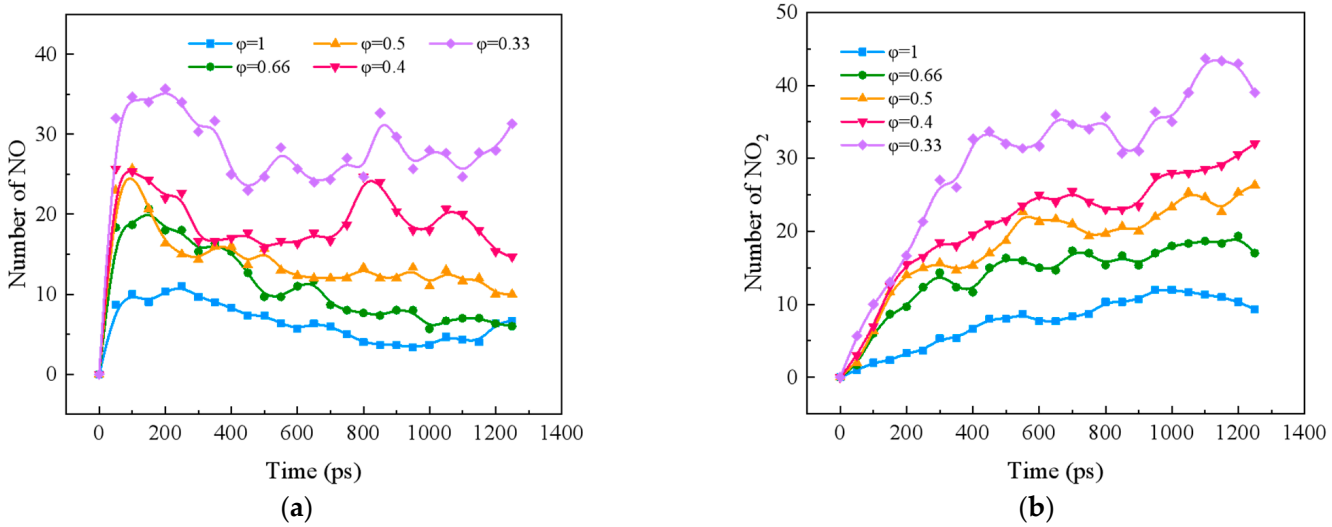

Figure 4. *Cont.*

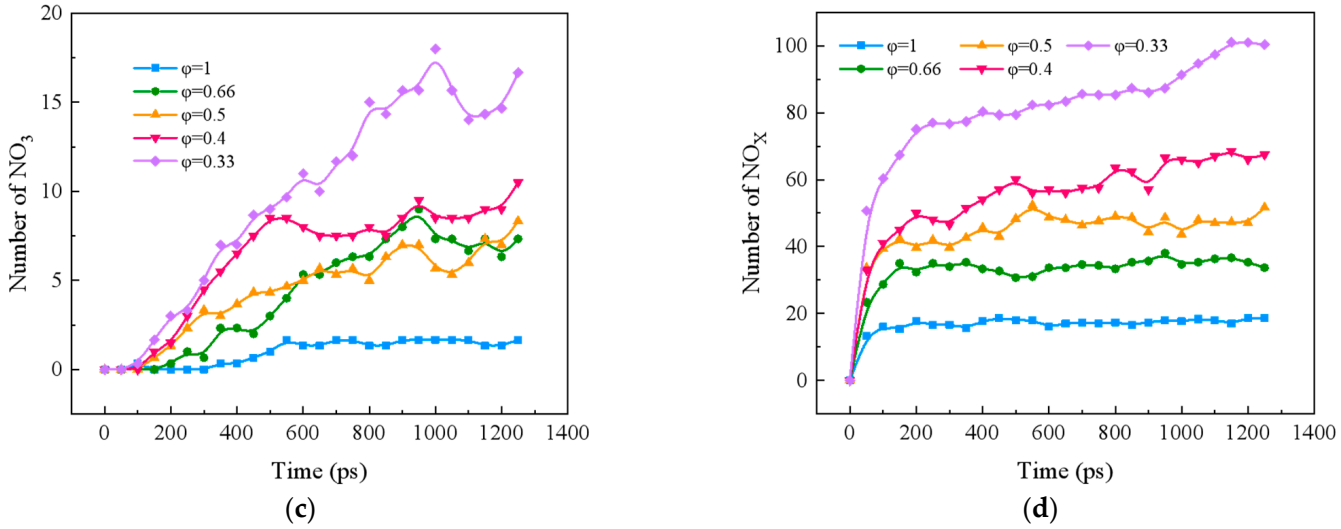

Figure 4. NO_X distribution during combustion of ternary carbon-neutral fuel blends with different equivalence ratios. (**a**) NO; (**b**) NO_2; (**c**) NO_3; (**d**) NO_X.

2.3. Mechanism Analysis of CO, CO_2, and NO_X Formation in the Combustion of Ternary Blended Fuel as Affected by Equivalence Ratio

In order to further discuss the impact of ternary blended fuel combustion on the mechanism of CO, CO_2, and NO_X formation as affected by the equivalence ratios, this paper generates reaction network diagrams for five operating conditions and discusses the N and C migration paths of ternary blended fuel combustion at different equivalence ratios as simulated using ReaxFF MD. Figure 5 represents the network diagrams of CO and CO_2 formation paths during the combustion of ternary carbon-neutral fuels at equivalence ratios of 1, 0.66, 0.5, 0.4, and 0.33, respectively. The percentage in the network diagram indicates the reactant conversion rate in order to highlight the main paths of the reaction network, and the reaction paths with a conversion rate of less than 15% are ignored in all network diagrams in this study.

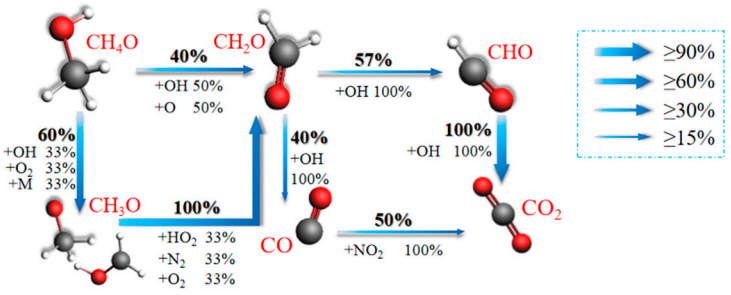

(**a**)

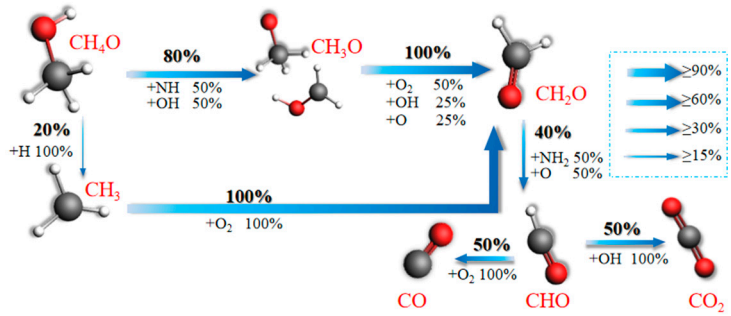

(**b**)

Figure 5. *Cont.*

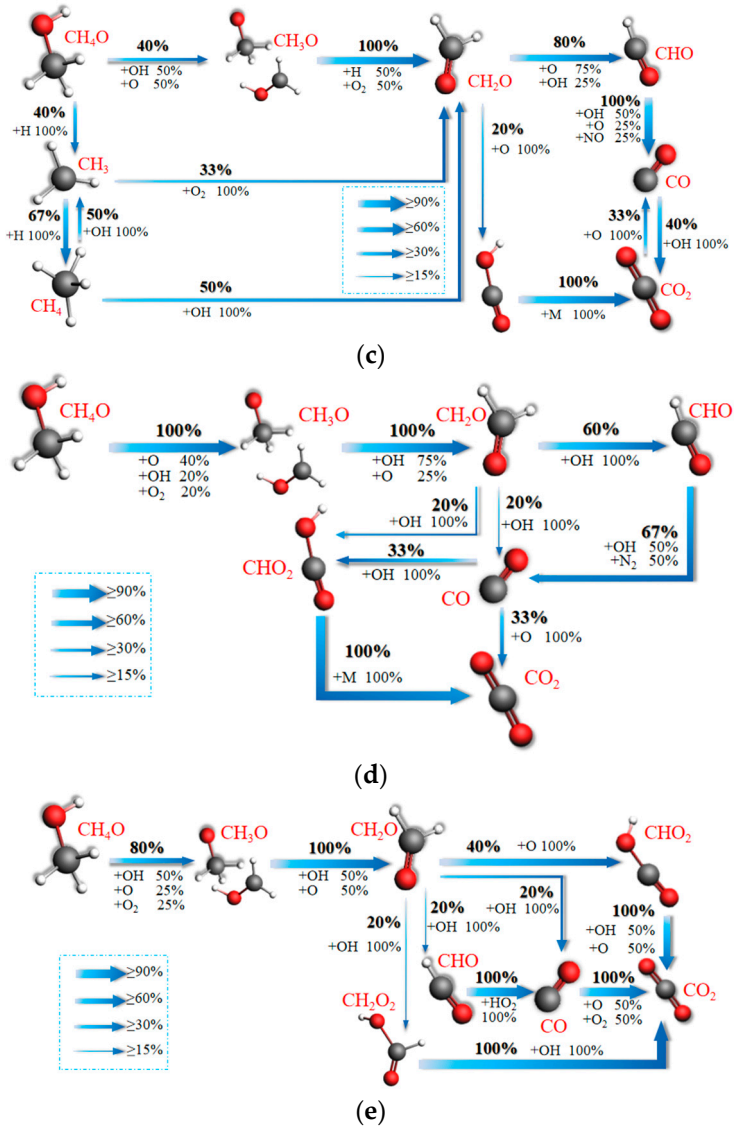

Figure 5. Main migration paths of C in ternary carbon-neutral fuel blends at different equivalence ratios. (**a**) φ = 1; (**b**) φ = 0.66; (**c**) φ = 0.5; (**d**) φ = 0.4; (**e**) φ = 0.33.

As can be seen in Figure 5a, all of the CH_4O is converted to CH_2O at φ = 1. A proportion of 40% of the CH_2O is generated as CO, and 77% of the CH_2O is converted to CO_2. This is consistent with the numerical ratios of CO and CO_2 in Section 2.2. From Figure 5b, it can be seen that all CH_4O is also converted to CH_2O at φ = 0.66. The difference with φ = 1 is that, in this case, CH_4O undergoes a direct reduction reaction with H, and this reaction produces CH_3. The conversion of CH_2O to CO and CO_2 in this case is both 20%.

As can be seen from Figure 5c, the complexity of the reaction path at φ = 0.5 is mainly reflected in the transition from CH_4O to CH_2O. There are three main paths in this part, which are: $CH_4O \rightarrow CH_3O \rightarrow CH_2O$, $CH_4O \rightarrow CH_3 \rightarrow CH_2O$, and $CH_4O \rightarrow CH_3 \rightarrow CH_4 \rightarrow CH_2O$. Among them, CH_3 and CH_4 can also be converted to each other. In terms of conversion rate, only 80% of CH_4O is converted to CH_2O through intermediates such as CH_3O, CH_3, and CH_4. Statistically, 69% of CH_4O is converted to CO. A total of 37% of CH_4O is converted to CO_2. From Figure 5d, it can be seen that all of the CH_4O is converted to CH_2O when φ = 0.4. The conversion rates of CH_2O to CO and CO_2 are 60.2% and 46.5%, respectively. From Figure 5e, it can be seen that at φ = 0.33, 80% of CH_4O is converted to CH_2O from CH_3O. The conversion rates of CH_4O to CO and CO_2 are 32% and 80%, respectively. The path diagram for this case is also complex, unlike at φ = 0.5, where

the complexity is mainly in the conversion phase of CH_2O to CO and CO_2. There are four main reaction paths in this stage, namely $CH_2O \rightarrow CHO_2 \rightarrow CO_2$, $CH_2O \rightarrow CO \rightarrow CO_2$, $CH_2O \rightarrow CHO \rightarrow CO \rightarrow CO_2$, and $CH_2O \rightarrow CH_2O_2 \rightarrow CO_2$.

Comparing with Figure 5, it is found that the number of pre-reaction paths increases as the equivalence ratio decreases for $\varphi \geq 0.5$. At $\varphi = 1$, there are only two paths from CH_4O to CH_2O, $CH_4O \rightarrow CH_2O$ and $CH_4O \rightarrow CH_3O \rightarrow CH_2O$. At $\varphi = 0.66$, the path of direct conversion of CH_4O to CH_2O disappears, and the new path $CH_4O \rightarrow CH_3 \rightarrow CH_2O$ is added. At $\varphi = 0.5$, the new path $CH_4O \rightarrow CH_3 \rightarrow CH_4 \rightarrow CH_2O$ is added compared with $\varphi = 0.66$. Combined with Figure 2d, this is because there is more H at $\varphi = 0.5$ and $\varphi = 0.66$. For $\varphi \leq 0.5$, the variety of paths in the later stages of the reaction increases as the equivalence ratio decreases. The intermediate CHO_2 is added at $\varphi = 0.5$ compared to $\varphi > 0.5$. The reaction paths from CH_2O to CO_2 are only $CH_2O \rightarrow CHO \rightarrow CO \rightarrow CO_2$ and $CH_2O \rightarrow CHO_2 \rightarrow CO_2$. The new paths $CH_2O \rightarrow CO \rightarrow CHO_2 \rightarrow CO_2$, $CH_2O \rightarrow CO \rightarrow CO_2$, and $CH_2O \rightarrow CHO \rightarrow CO \rightarrow CHO_2 \rightarrow CO_2$ are added at $\varphi = 0.4$ compared with $\varphi = 0.5$. The new paths $CH_2O \rightarrow CO \rightarrow CO_2$ and $CH_2O \rightarrow CH_2O_2 \rightarrow CO_2$ are added at $\varphi = 0.33$. Statistics show that the highest CO production rate is achieved at $\varphi = 0.5$. This validates the conclusion in Section 2.1 that the peak CO occurs at $\varphi = 0.5$. The equivalence ratios from 0.66 to 0.33 correspond to CO_2 production rates of 20%, 36.9%, 46.5%, and 80%, respectively. The increase with decreasing equivalence ratio is in line with the trend of CO_2 formation observed in Section 2.2. It was also found that the lowest CO and CO_2 production rates were both 20% at $\varphi = 0.66$, and their consumption rates were also the lowest. The combined analysis reveals that the lowest percentage of total CO and CO_2 remaining is found at $\varphi = 0.66$. Analyzed in conjunction with Figure 2c,d, this is the result of the higher H/OH ratio at $\varphi = 0.66$.

Figure 6 represents the network diagram of NO_X formation reaction paths in the combustion process of ternary fuels at equivalence ratios of 0.1, 0.66, 0.5, 0.4, and 0.33, respectively. As can be seen from the figure, all NO_X in the reaction is converted from NO. As can be seen from Figure 6a, the reaction generates more N_2 at $\varphi = 1$. There are four main paths of N_2 formation. They are $NH_3 \rightarrow N_2H_5 \rightarrow N_2$, $NH_3 \rightarrow NH_2 \rightarrow N_2H \rightarrow N_2$, $NH_3 \rightarrow NH_2 \rightarrow HNO \rightarrow N_2$, and $NH_3 \rightarrow NH_2 \rightarrow NH \rightarrow N_2$. This is a result of the fact that less OH radicals are generated by the lower O_2 at the high equivalence ratios. $NO \rightarrow HNO_2 \rightarrow NO_2$ is the main path in this case. From Figure 6b, 60% of NH_3 is converted to NO at $\varphi = 0.66$. $NH_3 \rightarrow NH_2 \rightarrow NH \rightarrow HNO \rightarrow NO \rightarrow HNO_2 \rightarrow NO_2$ is the main conversion path. Compared with $\varphi = 1$, a new pathway of NO_3 formation and consumption is added: $NH_3 \rightarrow NH_2 \rightarrow NH \rightarrow HNO \rightarrow NO \rightarrow HNO_2 \rightarrow NO_2 \rightarrow HNO_3 \rightarrow NO_3 \rightarrow NO_2$. From Figure 6c, it can be seen that at $\varphi = 0.5$, NH_3 is fully converted to NO through two different pathways: $NH_3 \rightarrow NH_2 \rightarrow HNO \rightarrow NO$ and $NH_3 \rightarrow NH \rightarrow HNO \rightarrow NO$. This also leads to the subsequent production of more NO_X. As can be seen from Figure 6d, the conversion of NH_3 to NO is reduced to 65% at $\varphi = 0.4$. There are also two main paths: $NH_3 \rightarrow NH_2 \rightarrow HNO \rightarrow NO$ and $NH_3 \rightarrow HNO \rightarrow NO$. The path from NH_3 to NO is shorter compared to that at $\varphi = 0.5$. From Figure 6e, the main path is $NH_3 \rightarrow NH_2 \rightarrow H_2NO \rightarrow NO \rightarrow HNO_2 \rightarrow NO_2 \rightarrow NO_3$ at $\varphi = 0.33$. The conversion rate of NH_3 to NO is 80%. The two conversion paths are $NH_3 \rightarrow NH_2 \rightarrow NO$ and $NH_3 \rightarrow HNO \rightarrow NO$. Fewer intermediates are required for the conversion of NH_3 to NO in this case than in other cases, and the conversion of NO to NO_3 is more direct: $NO \rightarrow NO_2 \rightarrow NO_3$.

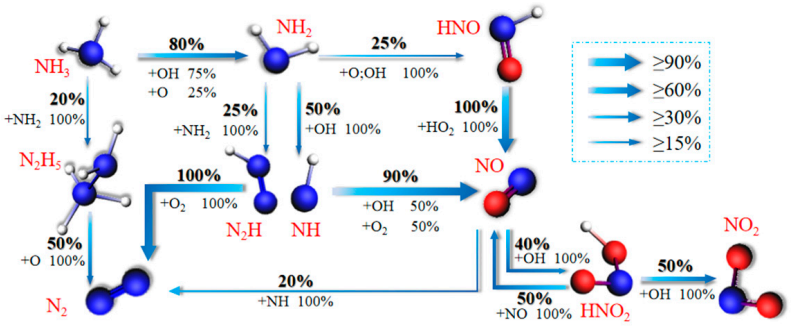

(**a**)

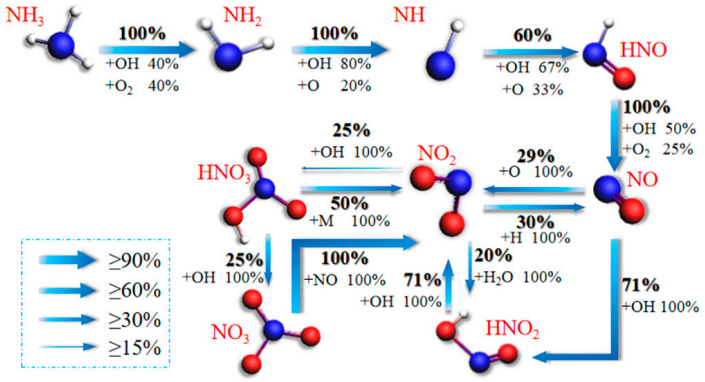

(**b**)

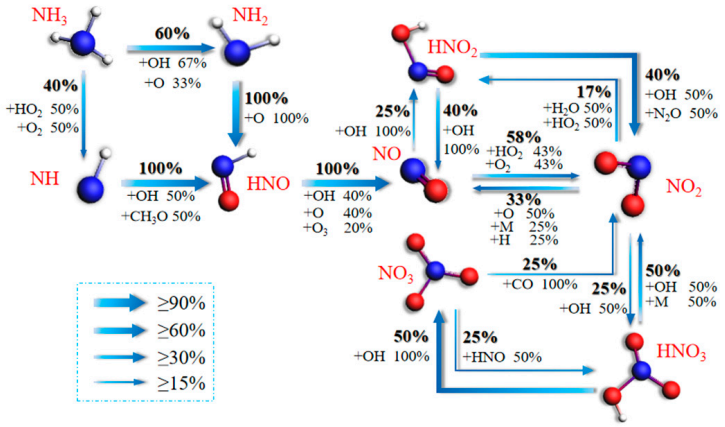

(**c**)

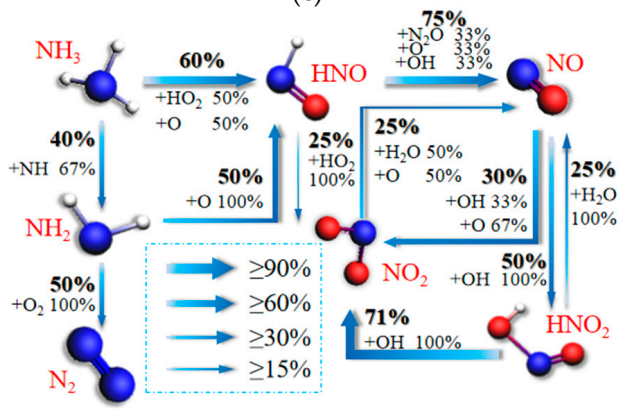

(**d**)

Figure 6. *Cont*.

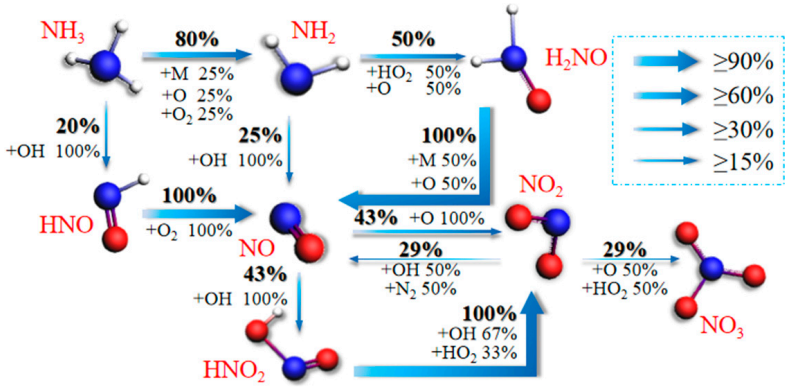

(**e**)

Figure 6. Main migration paths of N in ternary carbon-neutral fuel blends at different equivalence ratios. (**a**) φ = 1; (**b**) φ = 0.66; (**c**) φ = 0.5; (**d**) φ = 0.4; (**e**) φ = 0.33.

A comparison of Figure 6 shows that the main conversion path of NH3 to NO shifts from $NH_3 \rightarrow NH_2 \rightarrow NH \rightarrow NO$, $NH_3 \rightarrow NH_2 \rightarrow NH \rightarrow HNO \rightarrow NO$, and $NH_3 \rightarrow NH_2 \rightarrow HNO \rightarrow NO$ to $NH_3 \rightarrow HNO \rightarrow NO$ and $NH_3 \rightarrow NH_2 \rightarrow NO$ as the equivalence ratio decreases. The reaction path becomes progressively shorter, which is caused by more O_2 in the reaction as the equivalence ratio decreases. With more O_2, more OH and O radicals are produced in the reaction, and at low equivalence ratios, O_2 also participates directly in the reaction as a free radical. NO_2 is the main component of NO_X. Statistics show that the remaining proportions of NO_2 corresponding to equivalence ratios from 1 to 0.33 are 12%, 21.4%, 34%, 46.95%, and 48.86%, respectively. The remaining proportion of NO_2 increases with decreasing equivalence ratios, which explains the conclusion of Section 3.1 that the amount of NO_2 increases with decreasing equivalence ratios. The main reaction paths for each case are $NH_3 \rightarrow NH_2 \rightarrow NH \rightarrow NO \rightarrow HNO_2 \rightarrow NO_2$, $NH_3 \rightarrow NH_2 \rightarrow NH \rightarrow HNO \rightarrow NO \rightarrow HNO_2 \rightarrow NO_2 \rightarrow NO$, $NH_3 \rightarrow NH_2 \rightarrow HNO \rightarrow NO \rightarrow NO_2 \rightarrow NO$, $NH_3 \rightarrow HNO \rightarrow NO \rightarrow HNO_2 \rightarrow NO_2 \rightarrow NO$, and $NH_3 \rightarrow NH_2 \rightarrow H_2NO \rightarrow NO \rightarrow HNO_2 \rightarrow NO_2 \rightarrow NO_3$. Only φ = 0.33 contains NO3 production in the main pathway. Combined with the conversion analysis, the conversion of NH_3 to NO_3 is 0, 2.9%, 8.5%, 0, and 19.95%, respectively. This is due to the fact that there are more OH radicals in the tether at low equivalence ratios. It explains the observation in Section 2.1 that NO_3 is much higher at φ = 0.33 than other cases.

3. Materials and Methods

3.1. Reactive Force Field Molecular Dynamics (ReaxFF MD)

ReaxFF MD is a molecular dynamics simulation combined with the calculation of reaction force fields. Its reactive force field potential function is derived from experimental data and density functional theory, so the accuracy is close to quantum computation and does not require the predetermination of chemical reaction paths in the system [30]. ReaxFF MD has been widely used in the study of pyrolysis [31], combustion [32], explosions [33], oxidation [34], catalytic [35], and other systems involving physical chemistry. It provides a promising means of exploring the chemical behavior of complex molecular systems. Bond-order-dependent characterization is achieved through detailed parameterization of the atomic, bonding, angular, and torsional properties of each particle, and the interactions within the system [36]. The total energy of the system can be calculated by summing all partial energy terms as described in R1:

$$E_{system} = E_{bond} + E_{over} + E_{under} + E_{val} + E_{pen} + E_{tors} + E_{conj} + E_{vdWaals} + E_{coulomb} \quad (1)$$

where E_{bond}, E_{over}, E_{under}, E_{val}, E_{pen}, E_{tors}, and E_{conj} correspond to bond energy, over-coordination energy, under-coordination energy, bond angle energy, compensation energy, torsion energy, and four-body conjugation energy. The non-bonding terms mainly consist of van der Waals force energy ($E_{vdWaals}$) and Coulomb force energy ($E_{coulomb}$). When

calculating non-bonding interactions, the charged atoms cross the truncation radius of the non-bonding interactions, thus leading to a jump in energy. Therefore, the ReaxFF force field is additionally corrected by introducing a seventh-order polynomial Taper function, which ensures that at the truncation radius, the non-bonding interaction's first-, second-, and third-order derivatives of the energy term are all zero [37]. The ReaxFF force field also takes better account of charge polarization by employing the electronegativity equalization method [38] and updates the atomic charges at each time step [39]. The detailed meaning of the ReaxFF force field parameters, the setup of the molecular structure, and the applicability of the reaction force field have been described in detail in a previous study [40].

3.2. Case Set-Ups

Table 1 lists all the $CH_4O/H_2/NH_3$ blended combustion ReaxFF MD simulation cases under the high-pressure environment in this paper. The system density (ρ), temperature (T), and simulation time are 0.1 g/cm^3, 2000 K, and 1.25 ns, respectively. Cases 1 to 5 denote the combustion of $CH_4O/H_2/NH_3$ blends at fuel equivalent ratios (φ) of 0.5, 1, 0.66, 0.4, and 0.33, respectively. Each condition is calculated three times, keeping the initial settings constant. All results in this paper are averaged over three simulations. Through further comparative analyses, the mechanisms of CO, CO_2, and NO_X pollutant formation at different equivalence ratios are analyzed at the molecular level.

Table 1. ReaxFF MD cases of the $CH_4O/H_2/NH_3$ blended combustion.

Case	CH_4O	H_2	NH_3	O_2	N_2	ρ, g/cm^3	T, K	Φ
1	40	40	40	220	832	0.1	2000	0.5
2	40	40	40	110	416	0.1	2000	1
3	40	40	40	165	624	0.1	2000	0.66
4	40	40	40	375	1040	0.1	2000	0.4
5	40	40	40	330	1248	0.1	2000	0.33

3.3. Computational Details and Post-Processing

All the cases listed in Table 1 were carried out in the ReaxFF module of AMS [41–43]. In this study, the HE2.ff force field [44] and the regular system with constant atomic number, volume, and temperature (NVT) were used. To ensure the overall stability of hydrocarbon fuel combustion, the energy, and configuration of all simulated cases were first optimized using the "Geometry Optimization" and "Energy Optimization" plug-ins. Figure 7 shows the optimized systematic for case 1, which shows that the fuel and oxidant are uniformly blended, similar to a premixed flame, and similar to the cyclone burner we previously employed [45]. A Berendsen thermostat was used to control the temperature with a time step of 0.25 fs. Periodic boundary conditions were applied in all three xyz directions, and the soot intermediate components and product distributions were analyzed from trajectories using a 0.3 Å bond level cut-off.

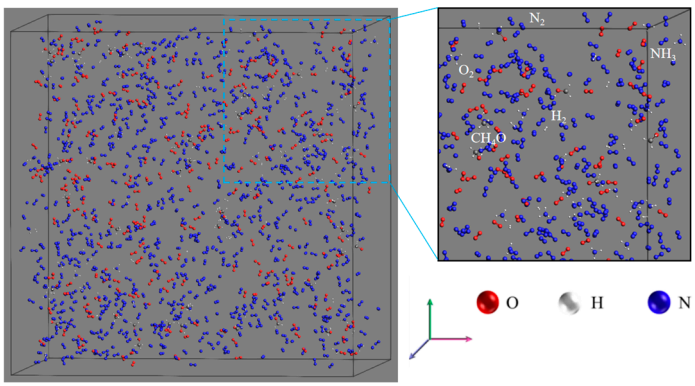

Figure 7. Optimization system for case 1.

3.4. Validation of the ReaxFF MD Method

The reliability and validity of the ReaxFF MD method have been widely used and verified in previous studies [36,37,46–49]. Among them, Wang et al. [36] constructed the reaction pathway of high-pressure combustion by tracking the trajectories of reacting atoms through ReaxFF MD. To understand the NO_X formation mechanism of NH_3/CH_4 combustion at different temperatures and pressures. The results showed that the high temperature accelerated the rate of NH_3 consumption, which was consistent with the experimental results. The high pressure complicated the reaction pathway of NH_3/CH_4 combustion through the emergence of new intermediates and primitive reactions. In addition, they pointed out that ReaxFF MD is a valuable tool for revealing the reaction mechanisms of combustion and pollutant formation in depth. Liu et al. [49] investigated the chemical reactivity effects of NO on the oxidation of CH_4 using ReaxFF MD simulations and found that increasing the blending ratio of NO accelerated the rate of CH_4 consumption. This is mainly due to the fact that, on the one hand, the conversion of NO to NO_2 generates OH radicals, which accelerates the CH_4 consumption; on the other hand, NO can also inhibit the CH_4 consumption by combining with reactive radicals. Wang et al. [46] applied ReaxFF MD and Py-GC/MS to investigate the characteristics of the soot particulate formation in the process of hydrogen-doped combustion of methane and ethylene, and both experimental and numerical results reflected that PAHs and ethylene were not the most important pollutants in the combustion process of CH_4. The experimental and numerical results reflect the evolution of PAHs and initial soot particles, as well as the different chemical effects of hydrogen doping on PAHs and soot formation.

4. Conclusions

In this paper, the effects of different reactant equivalence ratios on the combustion reaction rates and the formation characteristics of CO, CO_2, and NO_X pollutants during the combustion of $CH_4O/H_2/NH_3$ ternary carbon-neutral blended fuels have been investigated for the first time using ReaxFF MD. The mechanisms of CO, CO_2, and NO_X formation in ternary blended fuels with different equivalence ratios were investigated at the molecular level. The conclusions of this paper are summarized as follows:

(1) Reducing the equivalence ratio accelerates the decomposition of CH_4O, NH_3, and H_2 in general. The rate of consumption of each fuel is fastest at $\varphi = 0.33$. The rates of CH_4O and NH_3 decomposition are similar at $\varphi = 0.66$ and $\varphi = 0.4$.

(2) CO showed an "inverted U" shaped trend of increasing and then decreasing over time. The CO peak appeared at $\varphi = 0.5$. CO_2 shows a continuous increase as the reaction proceeds. The rate and amount of CO_2 formation are inversely proportional to the magnitude of the equivalence ratio. When $\varphi > 0.5$, the effect of equivalence ratio on CO_2 is more obvious. NO_2 is the main component of NO_X. When $\varphi \geq 0.66$, NO_X shows a tendency to increase and then stabilize as the reaction proceeds. When $\varphi < 0.66$, NO_X shows a continuous increasing trend.

(3) C migration path analysis showed that for $\varphi \geq 0.5$, the intermediates CH_3 and CH_4 are added to the CH_4O to CH_2O conversion stage as the equivalence ratio decreases. The new pathways are $CH_4O \rightarrow CH_3 \rightarrow CH_2O$ and $CH_4O \rightarrow CH_3 \rightarrow CH_4 \rightarrow CH_2O$. At $\varphi \leq 0.5$, new intermediates CHO_2 and CH_2O_2 are added to the CH_2O to CO_2 phase as the equivalence ratio decreases. The added paths are $CH_2O \rightarrow CO \rightarrow CHO_2 \rightarrow CO_2$, $CH_2O \rightarrow CO \rightarrow CO_2$, $CH_2O \rightarrow CHO \rightarrow CO \rightarrow CHO_2 \rightarrow CO_2$, and $CH_2O \rightarrow CH_2O_2 \rightarrow CO_2$.

(4) N migration pathway analysis showed that the conversion pathway of NH_3 to NO shifted from the long reaction chains of $NH_3 \rightarrow NH_2 \rightarrow NH \rightarrow NO$, $NH_3 \rightarrow NH_2 \rightarrow NH \rightarrow HNO \rightarrow NO$, and $NH_3 \rightarrow NH_2 \rightarrow HNO \rightarrow NO$, to the shorter reaction chains of $NH_3 \rightarrow HNO \rightarrow NO$ and $NH_3 \rightarrow NH_2 \rightarrow NO$ as the equivalence ratio decreased. This is due to the fact that as the equivalence ratio decreases, more O_2 collides to form OH and some of the O_2 is directly involved in the reaction. NO_2 is the main component of NO_X. Statistics show that the equivalence ratios from 1 to 0.33 correspond to 12%,

21.4%, 34%, 46.95%, and 48.86% of NO_2 remaining, respectively. This is also caused by the influence of the equivalence ratio on the OH radical concentration.

Author Contributions: J.S.: investigation, data curation, visualization, analysis, writing—original draft, writing—editing. Q.L.: investigation, data curation, visualization. M.G.: writing—review and editing. supervision, project administration, funding acquisition. Y.W.: analysis, writing—review, supervision. All authors have read and agreed to the published version of the manuscript.

Funding: This research was funded by the National Natural Science Foundation of China (52376008), the Natural Science Foundation of Anhui Province (2308085QE168), University synergy innovation program of Anhui province (GXXT-2022-025), and the Funding for Postdoctoral Researchers' Scientific Research Activities in Anhui Province (2023B718).

Institutional Review Board Statement: Not applicable.

Informed Consent Statement: Not applicable.

Data Availability Statement: Data are contained within the article.

Conflicts of Interest: The authors declare no conflicts of interest.

References

1. Jisoo, S.; Sungwook, P. Numerical analysis for optimizing combustion strategy in an ammonia-diesel dual-fuel engine. *Energy Convers. Manag.* **2023**, *284*, 116980.
2. Zhang, L.; Sun, R.; Wang, Z.; Zhu, W.; Wang, X.; Qi, H. Application of experiments and density function theory on the formation mechanism of NH during O/Ar and O/HO combustion process of demineralized coals. *Fuel* **2023**, *331*, 125730. [CrossRef]
3. Wang, J.; Li, X.; Li, J.; Xie, Y.; Fan, M.; Jiang, L. Study on the ignition characteristics of CH_4/H_2/air mixtures in a micro flow reactor with a controlled temperature profile. *Int. J. Hydrogen Energy* **2023**, *51*, 818–829. [CrossRef]
4. Yan, Z.; Yang, Y.; Li, Q.; Yan, Y.; Tian, Z.; Song, C.; Huang, Z. Study on effects of NH_3 and/or H_2 addition on the characteristics of soot formation and gas emissions in a laminar ethylene diffusion flame. *Fuel Process Technol.* **2023**, *242*, 107633. [CrossRef]
5. Xuan, J.; He, L.; Wen, W.; Feng, Y. Hydrogenase and Nitrogenase: Key Catalysts in Biohydrogen Production. *Molecules* **2023**, *28*, 1392. [CrossRef] [PubMed]
6. Wang, Y.; Gu, M.; Zhu, Y.; Cao, L.; Zhu, B.; Wu, J.; Lin, Y.; Huang, X. A review of the effects of hydrogen, carbon dioxide, and water vapor addition on soot formation in hydrocarbon flames. *Int. J. Hydrogen Energy* **2021**, *46*, 31400–31427. [CrossRef]
7. Zhang, F.; Li, S.; Liu, Q.; Sun, J.; Wei, X.; Gu, M.; Wang, Y.; Huang, X. Effect of ammonia on the soot surface characteristics in ammonia/ethylene co-flow diffusion flames. *Fuel* **2023**, *341*, 127633. [CrossRef]
8. Arun, K.; Ganesh, D.; Nagarajan, G.; Abul, K. An innovative method of ammonia use in a light-duty automotive diesel engine to enhance diesel combustion, performance, and emissions. *Int. J. Hydrogen Energy* **2020**, *45*, 98–118.
9. Xu, L.; Xu, S.; Bai, X.; Juho, A.; Saana, H.; Jari, H. Performance and emission characteristics of an ammonia/diesel dual-fuel marine engine. *Renew. Sust. Energy Rev.* **2023**, *185*, 113631. [CrossRef]
10. Sanchez, A.; Castellano, E.; Martín, M.; Vega, P. Evaluating ammonia as green fuel for power formation: A thermo-chemical perspective. *Appl. Energy* **2021**, *293*, 116956. [CrossRef]
11. Fenghour, A.; Wakeham, A.; Vesovic, V.; Watson, J.; Millat, J.; Vogel, E. The viscosity of ammonia. *J. Phys. Chem. Ref. Data* **1995**, *24*, 1649–1667. [CrossRef]
12. Frigo, S.; Gentili, R. Analysis of the behaviour of a 4-stroke Si engine fuelled with ammonia and hydrogen. *Int. J. Hydrogen Energy* **2013**, *38*, 1607–1615. [CrossRef]
13. Chai, W.; Bao, Y.; Jin, P.; Tang, G.; Zhou, L. A review on ammonia, ammonia-hydrogen and ammonia-methane fuels. *Renew. Sustain. Energy Rev.* **2021**, *147*, 111254. [CrossRef]
14. Zhang, R.; Chen, L.; Wei, H.; Li, J.; Chen, R.; Pana, J. Understanding the difference in combustion and flame propagation characteristics between ammonia and methane using an optical SI engine. *Fuel* **2022**, *324*, 124794. [CrossRef]
15. Nozari, H.; Karabeyouglu, A. Numerical study of combustion characteristics of ammonia as a renewable fuel and establishment of reduced reaction mechanisms. *Fuel* **2015**, *159*, 223–233. [CrossRef]
16. Charles, L.; Pierre, B.; Francesco, C.; Christine, M. Experimental investigation on ammonia combustion behavior in a spark-ignition engine by means of laminar and turbulent expanding flames. *Proc. Combust. Inst.* **2021**, *38*, 5859–5868.
17. Chen, D.; Li, J.; Li, X.; Deng, L.; He, Z.; Huang, H.; Noriyuki, K. Study on combustion characteristics of hydrogen addition on ammonia flame at a porous burner. *Energy* **2022**, *263*, 125613. [CrossRef]
18. Wang, S.; Li, Y.; Lv, J.; Liu, Z.; Gao, S.; Hu, J.; Zhang, J.; Zhong, J.; Zhao, Z. Evaluation of hydrogen addition on combustion and emission characteristics of dual-fuel diesel engines with different compression ratios. *Processes* **2023**, *11*, 2675. [CrossRef]
19. Kurien, C.; Mittal, M. Review on the production and utilization of green ammonia as an alternate fuel in dual-fuel compression ignition engines. *Energy Convers. Manag.* **2022**, *251*, 114990.

20. Wang, W.; Herreros, J.; Tsolakis, A.; York, A. Ammonia as hydrogen carrier for transportation; investigation of the ammonia exhaust gas fuel reforming. *Int. J. Hydrogen Energy* **2013**, *38*, 9907–9917. [CrossRef]
21. Alam, M.; Goto, M.; Sugiyama, S.; Kajiwara, K.; Mori, M.; Konno, M.; Motohashi, M.; Oyama, K. Performance and emissions of a DI diesel engine operated with LPG and ignition improving additives. *SAE Int. J. Engines* **2001**, *01*, 3680.
22. Miller, J.; Nagarajan, G.; Renganarayanan, S. LPG fueled diesel engine using diethyl ether with exhaust gas recirculation. *Int. J. Therm. Sci.* **2008**, *47*, 450–457. [CrossRef]
23. Karabektas, M.; Ergen, G.; Hosoz, M. The effects of using diethylether as additive on the performance and emissions of a diesel engine fuelled with CNG. *Fuel* **2014**, *115*, 855–860. [CrossRef]
24. Tomislav, P.; Martina, P.; Franjo, S.; Larisa, Z.; Tomaz, U. A Simple two-dimensional model of methanol. *J. Mol. Liq.* **2018**, *262*, 46–57.
25. Liu, M.; Dong, D.; Wei, F.; Long, W.; Wang, Y.; Cong, L.; Dong, P.; Tian, H.; Wang, P. Chemical mechanism of ammonia-methanol combustion and chemical reaction kinetics analysis for different methanol blends. *Fuel* **2023**, *314*, 127697. [CrossRef]
26. Wei, F.; Wang, Q.; Cao, J.; Cui, Z.; Long, W.; Tian, H. Experimental study of the ignition chamber with accelerating cavity applying to methanol lean combustion. *Fuel* **2024**, *355*, 129358. [CrossRef]
27. Li, X.; Ma, Z.; Jin, Y.; Wang, X.; Xi, Z.; Hu, S.; Chu, X. Effect of methanol blending on the high-temperature auto-ignition of ammonia: An experimental and modeling study. *Fuel* **2023**, *339*, 126911. [CrossRef]
28. Li, M.; He, X.; Hashemi, H.; Glarborg, P.; Lowe, V.; Marshall, P.; Fernandes, R.; Shu, B. An experimental and modeling study on auto-ignition kinetics of ammonia/methanol mixtures at intermediate temperature and high pressure. *Combust. Flame* **2022**, *242*, 112160. [CrossRef]
29. Hong, C.; Ji, C.; Wang, S.; Xin, G.; Wang, Z.; Meng, H.; Yang, J. An experimental study of various load control strategies for an ammonia/hydrogen dual-fuel engine with the Miller cycle. *Fuel Process Technol.* **2023**, *247*, 107780. [CrossRef]
30. van Duin, A.; Dasgupta, S.; Lorant, F.; Goddard, W.A. ReaxFF: A reactive force field for hydrocarbons. *J. Phys. Chem. A* **2001**, *105*, 9396–9409. [CrossRef]
31. Gao, M.; Li, X.; Guo, L. Pyrolysis simulations of Fugu coal by large-scale ReaxFF molecular dynamics. *Fuel Process Technol.* **2018**, *178*, 197–205. [CrossRef]
32. Cheng, Y.; Zhao, Y.; Zhao, F.; Xu, S.; Ju, X.; Ye, C. ReaxFF simulations on the combustion of Al and n-butanol nanofluid. *Fuel* **2022**, *330*, 125465. [CrossRef]
33. Zhang, M.; Zhou, B.; Chen, Y.; Gong, H. Mechanism and safety analysis of acetylene decomposition explosion: A combined ReaxFF MD with DFT study. *Fue* **2022**, *3227*, 124996. [CrossRef]
34. Li, Y.; Li, G.; Zhang, H.; Wang, J.; Li, A.; Liang, Y. ReaxFF study on nitrogen-transfer mechanism in the oxidation process of lignite. *Fuel* **2017**, *193*, 331–342. [CrossRef]
35. Li, Z.; Yang, Q.; Li, T.; Ma, X.; Zhou, J.; Ye, T.; Wu, J.; Wu, R.; Ben, H. Formation mechanism of hydrogen production from catalytic pyrolysis of waste tires: A ReaxFF molecular dynamics and experimental study. *Fuel* **2023**, *341*, 127664. [CrossRef]
36. Wang, J.; Jiang, X.; Luo, K. Exploring reaction mechanism for ammonia/methane combustion via reactive molecular dynamics simulations. *Fuel* **2023**, *331*, 125806. [CrossRef]
37. Kwon, H.; Shabnam, S.; van Duin, A.; Xuan, Y. Numerical simulations of yield-based sooting tendencies of aromatic fuels using ReaxFF molecular dynamics. *Fuel* **2020**, *262*, 116545. [CrossRef]
38. Mortier, W.; Ghosh, S.; Shankar, S. Electronegativity equalization method for the calculation of atomic charges in molecules. *Cheminform* **1986**, *108*, 4315–4320. [CrossRef]
39. Chenoweth, K.; van Duin, A.; Goddard, W. ReaxFF reactive force field for molecular dynamics simulations of hydrocarbon oxidation. *J. Phys. Chem. A* **2008**, *112*, 1040–1053. [CrossRef]
40. Bhoi, S.; Banerjee, T.; Mohanty, K. Molecular dynamic simulation of spontaneous combustion and pyrolysis of brown coal using ReaxFF. *Fuel* **2014**, *136*, 326–333. [CrossRef]
41. Lele, A.; Kwon, H.; Ganeshan, K.; Xuan, Y.; van Duin, A. ReaxFF molecular dynamics study on pyrolysis of bicyclic compounds for aviation fuel. *Fuel* **2021**, *297*, 120724. [CrossRef]
42. Senda, T.; Yamada, Y.; Morimoto, M.; Nono, N.; Sogabe, T.; Kubo, S.; Sato, S. Analyses of oxidation process for isotropic pitch-based carbon fibers using model compounds. *Carbon* **2019**, *142*, 311–326. [CrossRef]
43. Wang, Y.; Gong, S.; Wang, H.; Li, L.; Liu, G. High-temperature pyrolysis of isoprenoid hydrocarbon p-menthane using ReaxFF molecular dynamics simulation. *J. Anal. Appl. Pyrol.* **2021**, *155*, 105045. [CrossRef]
44. Zhang, L.; Zybin, S.; van Duin, A.; Dasgupta, S.; GoddardIII, W. Carbon cluster formation during thermal decomposition of octahydro-1,3,5,7-tetranitro-1,3,5,7-tetrazocine and 1,3,5-Triamino-2,4,6-trinitrobenzene high explosives from ReaxFF reactive molecular dynamics simulations. *J. Phys. Chem. A* **2009**, *113*, 10619–10640. [CrossRef] [PubMed]
45. Lin, Q.; Jiang, Y.; Liu, C.; Chen, L.; Zhang, W.; Ding, J.; Li, J. Controllable NO emission and high flame performance of ammonia combustion assisted by non-equilibrium plasma. *Fuel* **2022**, *319*, 123818. [CrossRef]
46. Wang, Y.; Gu, M.; Zhu, Y.; Cao, L.; Wu, J.; Lin, Y.; Huang, X. Analysis of soot formation of CH_4 and C_2H_4 with H_2 addition via ReaxFF molecular dynamics and pyrolysis–gas chromatography/mass spectrometry. *J. Energy Inst.* **2022**, *100*, 177–188. [CrossRef]
47. Chen, Z.; Sun, W.; Zhao, L. High-temperature and high-pressure pyrolysis of hexadecane: Molecular dynamic simulation based on reactive force field (ReaxFF). *J. Phys. Chem. A* **2017**, *121*, 2069–2078. [CrossRef]

48. Senftle, T.; Hong, S.; Islam, M.; Kylasa, S.; Zheng, Y.; Shin, Y.; Junkermeier, C.; Engel-Herbert, R.; Janik, J.; Aktulga, H.M.; et al. The ReaxFF reactive force-field: Development, applications and future directions. *NPJ Comput. Mater.* **2016**, *2*, 15011. [CrossRef]
49. Liu, Y.; Zhang, X.; Ding, J. Chemical effect of NO on CH_4 oxidation during combustion in O_2/NO environments. *Chem. Phys. Lett.* **2019**, *727*, 59–65. [CrossRef]